Intravital imaging of tumour vascular networks using multi-photon fluorescence microscopy

Gillian M. Tozer[a,*], Simon M. Ameer-Beg[b], Jennifer Baker[a], Paul R. Barber[b], Sally A. Hill[a], Richard J. Hodgkiss[b], Rosalind Locke[b], Vivien E. Prise[a], Ian Wilson[a], Borivoj Vojnovic[b]

[a]Tumour Microcirculation Group, Gray Cancer Institute, P. O. Box 100, Mount Vernon Hospital, Northwood, Middlesex HA6 2JR, UK
[b]Advanced Technology Development Group, Gray Cancer Institute, P. O. Box 100, Mount Vernon Hospital, Northwood, Middlesex HA6 2JR, UK

Abstract

The blood supply of solid tumours affects the outcome of treatment via its influence on the microenvironment of tumour cells and drug delivery. In addition, tumour blood vessels are an important target for cancer therapy. Intravital microscopy of tumours growing in 'window chambers' in animal models provides a means of directly investigating tumour angiogenesis and vascular response to treatment, in terms of both the morphology of blood vessel networks and the function of individual vessels. These techniques allow repeated measurements of the same tumour. Recently, multi-photon fluorescence microscopy techniques have been applied to these model systems to obtain 3D images of the tumour vasculature, whilst simultaneously avoiding some of the problems associated with the use of conventional fluorescence microscopy in living tissues. Here, we review the current status of this work and provide some examples of its use for studying the dynamics of tumour angiogenesis and vascular function.
© 2004 Elsevier B.V. All rights reserved.

Keywords: Vascular morphology; Vascular permeability; Vascular targeting; Tumour angiogenesis; Multi-photon microscopy; Intravital microscopy

Contents

* Corresponding author. Tel.: +44 1923 828611; fax: +44 1923 835210.
E-mail address: tozer@gci.ac.uk (G.M. Tozer).

1. Introduction

The blood supply of solid tumours plays a critical role in cancer therapy. Blood flow rate within individual vessels, intercapillary distances and vascular permeability are key parameters dictating the efficiency of drug delivery to tumours. Most solid tumours vascularize via angiogenesis, the process by which new blood vessels develop from pre-existing ones. The angiogenic "switch" is triggered by micro-environmental changes such as the development of hypoxia, which occur as the solid tumour grows. These changes result in an increased production of pro-angiogenic, as opposed to anti-angiogenic, growth factors such as vascular endothelial growth factor (VEGF), which induce the proliferation and migration of vascular endothelial cells [1]. The angiogenic process is complex and under tight molecular control, which has been reviewed elsewhere [2]. Once established, the tumour vasculature differs markedly from that in the host tissue. The vascular wall is poorly developed, often with a discontinuous endothelial cell lining, relatively poor investiture with vascular smooth muscle cells or pericytes [3,4] and an irregular basement membrane [5]. These features contribute to a high intrinsic vascular permeability to macromolecules [6,7], with development of high interstitial fluid pressure [8]. Tumour vascular networks also feature complex branching patterns and lack of hierarchy [9–11]. The result is a high geometrical resistance to blood flow leading to both spatial and temporal heterogeneity in blood flow rate [12,13]. In turn, these characteristics lead to a sub-population of tumour cells existing in a microenvironment featuring hypoxia, low pH and substrate depletion, which triggers further angiogenesis and selection for an aggressive phenotype [14]. Hypoxia is classically associated with resistance to radiotherapy but is also a marker for poor prognosis in a number of other treatment settings [15,16].

In the light of these considerations, it is clear that the tumour vasculature influences the outcome of treatment. In addition, the tumour vasculature is an attractive target for therapy because of its accessibility to blood-borne anti-cancer agents, the reliance of most tumour cells on an intact vascular supply for their survival and its role as a major route for metastatic spread [2,17,18]. For research in these areas, it is essential to measure both morphological and functional parameters of the tumour vasculature in vivo.

Specialized sites for tumour transplantation allow optical access to tumours in vivo for dynamic studies (intravital microscopy). This usually involves surgical implantation, in the dorsal skin [19] or cranium [20], of a metal or plastic frame supporting either a single- or double-sided glass coverslip (window chamber), through which the growing tumour can be observed microscopically. Conventional trans-illumination and fluorescence imaging of such preparations yields valuable information in the focal plane, although the presence (or absence) of out-of-plane objects can lead to ambiguity in determinations of such parameters as

inter-capillary distance, vessel lengths, branching ratios and leakage of fluorescent markers. Accurate determination of the complete three-dimensional vascular matrix is therefore desirable. In this article, we describe the application of multi-photon fluorescence microscopy to studies of the morphology and function of tumour blood vessels in situ, in dorsal skin flap window chambers. As examples, we compare the morphological characteristics of two tumour types, with different sensitivities to the tumour vascular targeting agent, combretastatin A-4 3-O-phosphate (CA-4-P), and the effect of this agent on tumour vascular permeability.

2. Multi-photon fluorescence microscopy of living tissues

Until recently, detailed three-dimensional information about the structure and organisation of vasculature in tumours and normal tissues was only obtainable from serial reconstruction of thin histological sections [21] or from vascular casting techniques [11], both of which are incompatible with repeated observation of living material. Confocal microscopical observations [22,23] of the vasculature can be carried out, where preparations are thin or prepared ex vivo. However, these techniques are not ideally suited to the imperfect optical conditions of living tissue because excessive deposition of excitation energy outside the focal plane causes bleaching of chromophores and other photo-damage and the short wavelengths used are susceptible to scattering and to changes in refractive index in different tissue compartments. A technique, which shows considerable promise for non- (or minimally) invasive three-dimensional biological imaging, is multi-photon microscopy [24]. The particular advantage of multi-photon imaging resides in the use of intense near-infrared (NIR) light to induce non-linear absorption in a probe fluorophore. That is to say, that excitation of the fluorophore is only achieved where simultaneous absorption of two or more photons occurs. The non-linear absorption is proportional to the intensity to the power n (where n is the number of photons absorbed by the fluorophore, typically 2), thereby confining the excitation to the vicinity of the focal plane of the imaging lens. This inherent sectioning capability allows the collection of three-

dimensional data without the use of a confocal aperture (since fluorescence is generated only in the focal volume, allowing simplified detection systems to be employed [25]). Since NIR is inherently scattered to a lesser degree than visible light (Rayleigh scattering $\propto$ wavelength^{-4}) and linear absorption of the NIR is low for most biological applications, thick (ca. 500 μm) samples may be imaged [26]. Photobleaching and photodamage are also greatly reduced due to the confinement of excitation to the focal volume [27]. In practice, efficient excitation of a fluorophore is obtained using NIR at approximately twice the wavelength (two-photon excitation) of that required in conventional fluorescence microscopy (one-photon excitation).

In some cases, the inherent sectioning ability of multi-photon microscopy is its greatest disadvantage; that is to say, that one cannot (as with confocal microscopy) simply open-up the collection pin-hole and observe a greater depth of field (albeit whilst reducing the lateral resolution). In addition, the acquisition of high resolution three-dimensional data sets is very time-consuming and typically limited by both the scan rate of the multi-photon microscope (although video rate systems are now available) [28,29] and the excitation powers that can be readily employed without significant photo-damage or toxicity.

A plethora of biological applications for multi-photon microscopy has been identified [30–32], although it should be pointed out that current technological limitations do restrict these in vivo applications to readily accessible sites such as the skin [33], the eye [34] and window chamber preparations for tumours. The key advantage of multi-photon microscopy for investigation of tumour vascular structure and function in vivo lies in its ability to obtain three-dimensional resolution at depth within the tumour. In addition, dynamic experiments, following tumour development, angiogenesis, treatment and resultant vascular remodelling, are possible at multiple time-points without compromising the model. In practice, measurement of gene expression, angiogenesis, drug delivery and vascular permeability has been demonstrated possible [35–39]. We have also demonstrated the utility of multi-photon microscopy for imaging fluorescence lifetime within the intra- and extravascular compartments of tumours in vivo and developed methods for quantifying vascular parame-

ters from 3D multi-photon images of tumour vascular networks [36,40,41].

3. Therapeutic targeting of the tumour vasculature with combretastatin A-4 3-*O*-phosphate (CA-4-P)

CA-4-P is currently in clinical trial as a tumour vascular targeting agent [42]. It is a tubulin binding agent structurally related to colchicine that causes rapid depolymerization of cytoskeletal microtubules in endothelial cells. Rapid signalling from the tubulin to the actin cytoskeleton results in re-organization of the actin cytoskeleton of endothelial cells in culture, resulting in cells rounding up and actin blebbing at cell margins [43]. These changes are thought to relate to an increase in vascular permeability and the very rapid and extensive decrease in blood flow, commonly observed in tumours in vivo [44]. The P22 rat sarcoma has previously been shown to be relatively sensitive to CA-4-P [45,46]. However, some tumour models, such as the HT29 human colorectal adenocarcinoma, grown as a xenograft in immuno-compromised (SCID) mice are relatively insensitive to CA-4-P and similar agents [44,47]. It is important to identify the vascular features that determine tumour sensitivity to CA-4-P in order to develop second-generation vascular targeting drugs and to predict which tumours will respond to these agents in the clinic. We have developed a multi-photon fluorescence microscopy technique for this purpose, following intravenous administration of fluorescently labelled 70 kDa dextran. In this review, we present data comparing the vascular features of the P22 tumour growing in its syngeneic host (BDIX rat) with those of the same tumour and the HT29 tumour growing in SCID mice.

Multi-photon techniques are amenable to measurement of vascular function as well as morphology and we have used it for investigating the permeability of tumour blood vessels to macromolecules. The tumour vasculature is characterized by its high permeability for plasma solutes, including proteins, which leads to the development of high interstitial fluid pressure. This is thought to be a barrier to the uniform tumour uptake of high molecular weight anti-cancer agents, which are highly dependent on convection for transport across the vascular wall and through the interstitium [48]. An increase in vascular permeability

is thought to be an early step in the development of new tumour blood vessels from pre-existing vessels (angiogenesis) and its measurement may therefore not only provide an insight into this process but also a means of detecting an early response to treatments designed to inhibit tumour angiogenesis. Tumour vascular permeability is therefore an important parameter to measure in tumour biology. More specifically, an increase in tumour vascular permeability is thought to be an important step in tumour vascular shutdown following CA-4-P treatment [44] and pretreatment vascular permeability may also be a predictive factor for response to treatment [47]. In this review, we illustrate the utility of multi-photon fluorescence microscopy for investigations of tumour vascular permeability by measuring the effect of CA-4-P treatment on leakage rate of FITC-labelled 40 kDa dextran from the vasculature of the P22 rat tumour. Extrapolation of the data to calculation of tumour vascular permeability to 40 kDa dextran is discussed. In all these experiments, tumours were grown in surgically implanted transparent dorsal skin flap window chambers and images obtained in the living animal, as described in Appendix A.

4. Experimental approaches to study tumour vascular networks by multi-photon fluorescence microscopy

4.1. The multi-photon microscope

For the studies presented here, microscopy was performed using a multi-photon microscope system based on a modified Bio-Rad MRC 1024MP workstation, comprising a solid-state-pumped (10 W Millennia X, Nd:YVO$_4$, Spectra-Physics), self-mode-locked Ti:Sapphire (Tsunami, Spectra-Physics) laser system, a-focal scan-head, confocal detectors and an inverted microscope (Nikon TE200) [36]. Enhanced detection of the scattered component of the emitted (fluorescence) photons is afforded by the use of three, in-house developed, non-descanned detectors, situated in the re-projected pupil plane (re-imaged objective back aperture). Due to geometrical constraints of the animal models, non-ideal long working distance objectives must be used and, here, a 10× Nikon Plan Fluor objective was used (16 mm

WD, 0.3 NA) for in vivo imaging. Excitation of both Cascade Blue™ and FITC fluorescence was possible using two-photon absorption at 800 or 890 nm (where indicated in the text) and isolated from background auto-fluorescence due to endogenous fluorophores using 455 and 540 nm filters (30 nm bandpass), respectively. Stacks of images of the tumour vasculature were acquired using Bio-Rad software and stored for off-line analysis. Details of the imaging techniques are described in Appendix B.

4.2. Measurement of morphological vascular parameters

Morphological vascular parameters were measured in tumours growing in both rats and mice, as described above. The first step towards quantification is delineation of tumour vascular networks in three-dimensional multi-photon images. In our experiments, this was achieved with tracing software (3D Trace) developed in-house [40,41] and illustrated in Fig. 1. This entailed manual and semi-automatic tracing through the data sets combined with automatic vessel diameter measurement. The traced networks were then represented by a list of points, each with an associated diameter, a sufficient number of points being required to ensure that a straight line joining adjacent points approximated the true course of the vessel. Distinct vessels were defined to be lengths of vasculature between branching points. These representations of the networks were used to calculate statistics and could also be used to recreate the networks in the Virtual Reality Modelling Language (VRML) such that they can be visualised by 3D
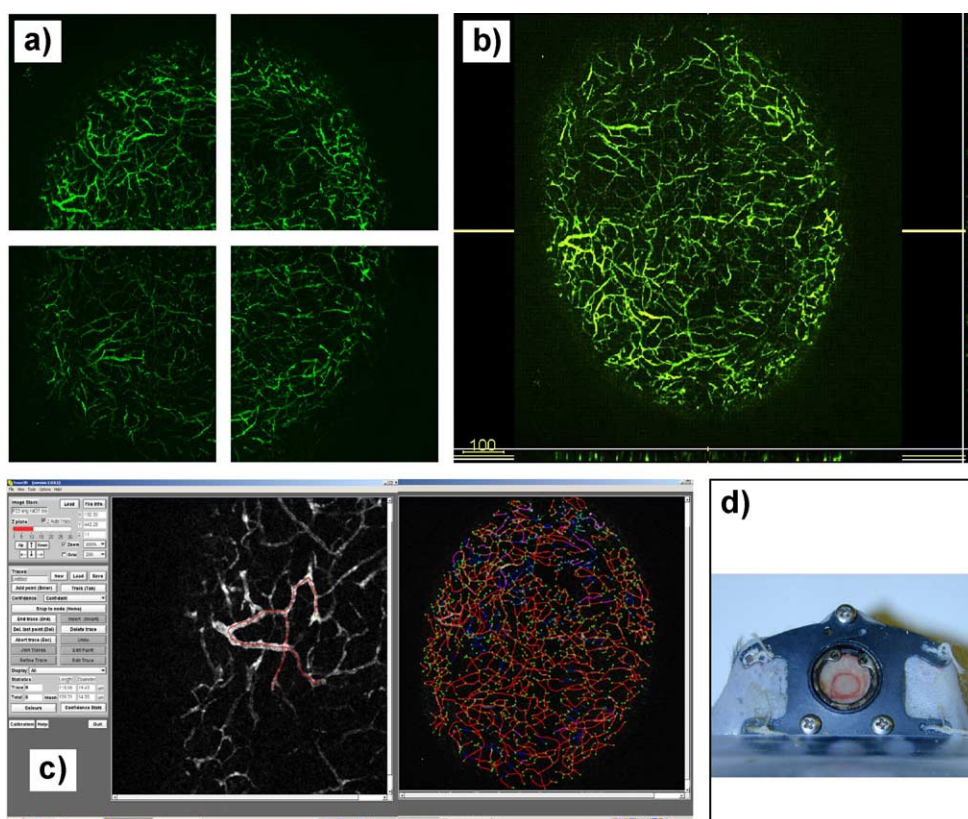
Fig. 1. Vascular delineation in a P22 tumour. Image (a) shows original volume-rendered data before stitching. Each panel measures 1.3×1.3 mm. Image (b) shows the stitched data. Image (c) shows a detail of the tumour vasculature during the vessel tracing procedure and the final traced image. Red traces indicate a higher level of confidence than blue traces and the green nodes represent vessel branching points. Image (d) shows a tumour growing in a dorsal skin-flap window chamber in a mouse.

surface-rendering software and visually compared to the volume-rendered data sets.

Several different statistics were collected. As well as straightforward statistics of vascular length, diameter, surface area and volume, the more complex measurements of tortuosity, interstitial distance to the nearest vessel and fractal dimension were made, as described in Appendix C.

4.3. Assessment of vascular permeability

Multi-photon microscopy provides a means of precisely localizing fluorescence within a three-dimensional image, thus avoiding out-of-focus fluorescence, which is a significant complication for quantifying vascular leakage of a fluorescent marker in conventional fluorescence microscopy [49]. In the current study, tumour vascular leakage of a purified 40 kDa dextran conjugated to fluorescein (FITC–dextran, Sigma) was measured in the P22 tumour growing in dorsal skin-flap window chambers implanted into rats. Intravascular tissue was delineated in 3D within sample regions of each image stack, so that fluorescence intensity within intravascular and extravascular tumour tissue could be measured over time following injection of the fluorophore. These leakage data were used to calculate the clearance constant K_i for the dextran, in rats treated with either 30 mg/kg CA-4-P or the equivalent volume of saline. K_i equates to the apparent tumour vascular permeability–vascular surface area product (*PS*). Details of these techniques are given in Appendix D.

5. Dynamics of the tumour microcirculation

5.1. Repeated imaging of the tumour vasculature

Fig. 2 shows a typical volume-rendered vascular network from a P22 rat tumour growing in a dorsal skin-flap window chamber. This figure illustrates the potential for multi-photon fluorescence excitation techniques for repeated measurements within the same vascular network. Fresh administration of the vascular marker was required each day, as most of it was cleared from the bloodstream within a 24-h period. However, there was some carry-over of the Cascade Blue–dextran conjugate from day 1 to day

2, resulting in an elevated, somewhat punctillate background fluorescence compared with that recorded on day 1. To avoid this problem, we imaged the vasculature on day 3 using the green fluorescence from a fluorescein–dextran conjugate, with a suitable emission filter to exclude blue fluorescence from any residual Cascade Blue–dextran marker. Qualitative comparison of the day 3 image in Fig. 2 and a second tumour region, which was only imaged on day 3, did not reveal any obvious differences in vessel number or appearance, suggesting that there were no gross vascular changes associated with repeated imaging (data not shown). However, functional assessment of the vasculature would need to be carried out to determine whether there are subtle vascular effects associated with this procedure.

Development and remodelling of the vasculature could be seen between day 1 (Fig. 2a) and subsequent days (Fig. 2b–d), although most of the vascular features remained constant over this time-course. The most obvious change in the imaged region was an increase in size of some individual vessels, rather than development of new vasculature In several cases where there was an apparent appearance of new blood vessels, careful inspection of images revealed that extremely thin blood vessels were present on day 1, as precursors of the enlarged vessels seen later. In other cases, individual vessels appeared to get narrower over the time-course of the experiment. In one example indicated by the arrow in Fig. 2, an initial small and highly twisted vessel grows progressively wider from day 1 to day 3, whilst retaining its twisted morphology. This vascular remodelling during tumour progression has received very little attention but may be extremely important for its effects on treatment outcome. For instance, such twisted regions of tumour blood vessels could impose very high stresses on the vascular wall leading to an imperfectly formed leaky structure. Whilst vessel remodelling is the most prominent feature in the sequence shown in Fig. 2, development of new vasculature at the expanding edge of a tumour can be observed in a similar way. Such studies have been performed in window chamber tumours using conventional transmitted and epi-fluorescence light microscopy [50,51], and multi-photon microscopy [35].
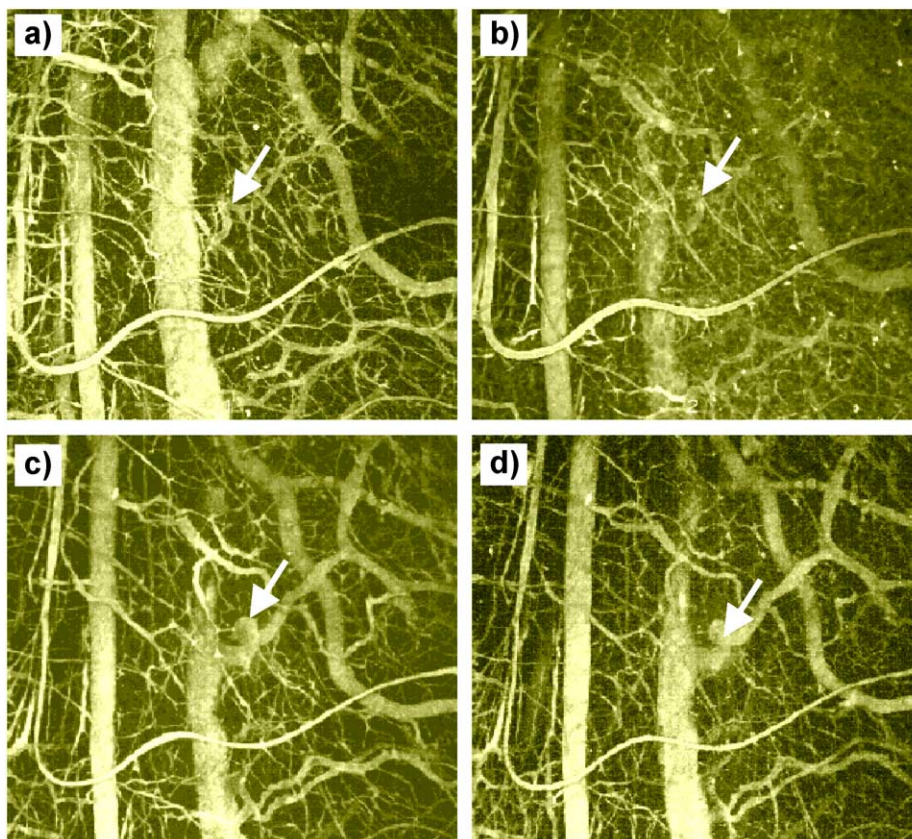
Fig. 2. Repeat imaging of the P22 tumour vasculature over 3 days. x–y co-ordinates recorded from the stage micrometer vernier scale were used to re-visit the same single region of the tumour on subsequent days. Each image was reconstructed from a stack of 51 serial images spaced 2 μm apart, representing a 100-μm-thick optical section. (a) Day 1; (b) day 2; (c) day 3 am; (d) day 3 pm, 4 h after the first image. Mean vessel diameter in the P22 tumour is approximately 13 μm. Arrow indicates a site of vascular remodelling.

5.2. Vascular networks in different tumour types

Fig. 3 shows typical examples of HT29 and P22 tumour vascular networks. Qualitatively, the most obvious difference between the tumour types is that the blood vessels in the HT29 tumours are often observed to orientate along the tumour radii, whereas the arrangement in the P22 tumours is much more uniform. Quantitative analysis of all the tumours in the study was carried out from surface-rendered images such as those illustrated in Fig. 3, following the vessel tracing procedure illustrated in Fig. 1 and automated vessel diameter measurements. The main purpose of this analysis was an attempt to identify morphological parameters, which could potentially explain the sensitivity of the P22 tumour versus the

resistance of the HT29 tumour to the vascular targeting drug, CA-4-P.

Figs. 4–7 show the results for the morphological analysis of vascular networks in the P22 and HT29 tumours. There were no obvious differences between the vascular development of the P22 tumour in its syngeneic rat host and in the SCID mouse, although more data in the mouse would be needed to confirm this assertion. There were some obvious relationships between several morphological parameters and tumour size for both tumour types. Fig. 4 shows that the average length of individual vessels tends to increase with tumour size, whereas the average diameter does not. Consequently, the average surface area and volume of vessels also tend to increase with tumour size (Fig. 5), although this relationship is less
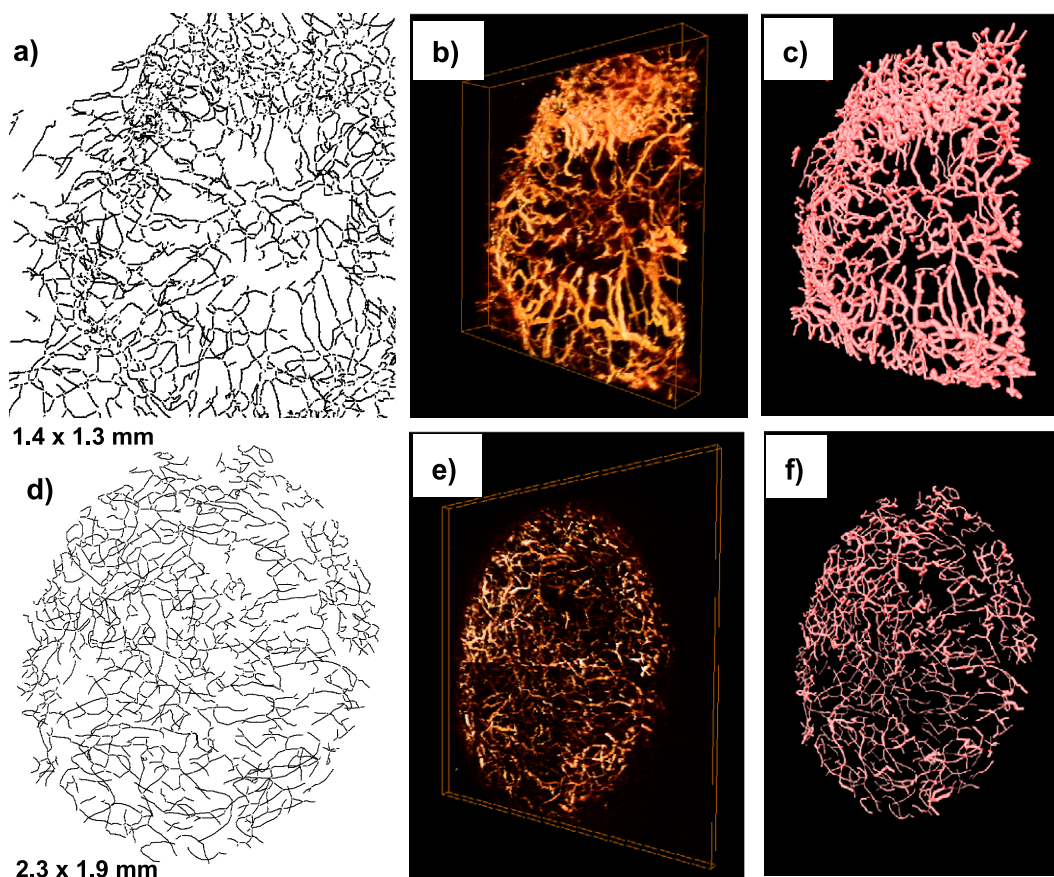
Fig. 3. 3D image re-construction for representative HT29 (a, b and c) and P22 (d, e and f) tumours. Dimensions represent the maximum and corresponding orthogonal tumour diameters in the x–y plane. Images (a) and (d) show all vascular traces projected onto the 2D x–y plane. Images (b) and (e) show the original volume-rendered data, (c) and (f) show the surface-rendered images of vascular networks following vascular tracing and diameter measurements.

apparent than that for average length because of the influence of diameter on the calculations. The fact that diameters, on average, remain constant as vessels lengthen can be interpreted in a number of ways. Firstly, it suggests an active process, rather than (or in addition to) a physical stretching effect, which might occur as a result of proliferation of surrounding tumour cells. This active process may involve vaso-dilation and/or remodelling of the vascular wall to maintain vessel diameter. In any case, these data suggest that the tumour vasculature adapts in an attempt to maintain its blood supply as the tumour grows. Fig. 6 illustrates this effect for these window chamber tumours. The vessel density clearly decreases with tumour size, suggesting that angio-genesis is out-paced by tumour cell proliferation.

However, as shown by the plots of vessel length density, surface area density and volume density (% vascular volume), the potentially catastrophic effect of a decreasing vascular density on the tumour's blood supply is offset by the lengthening of individual vessels and accompanying maintenance of vessel diameters. These results mask any variations in diameter within individual vessels over time but are consistent with the qualitative changes observed in tumours that were repeatedly imaged on consecutive days, which showed both temporal increases and decreases in diameter of individual vessel, as illustrated in Fig. 2.

Despite the qualitative differences in the vascular networks between HT29 and P22 tumours, there were few differences in the measured vascular parameters
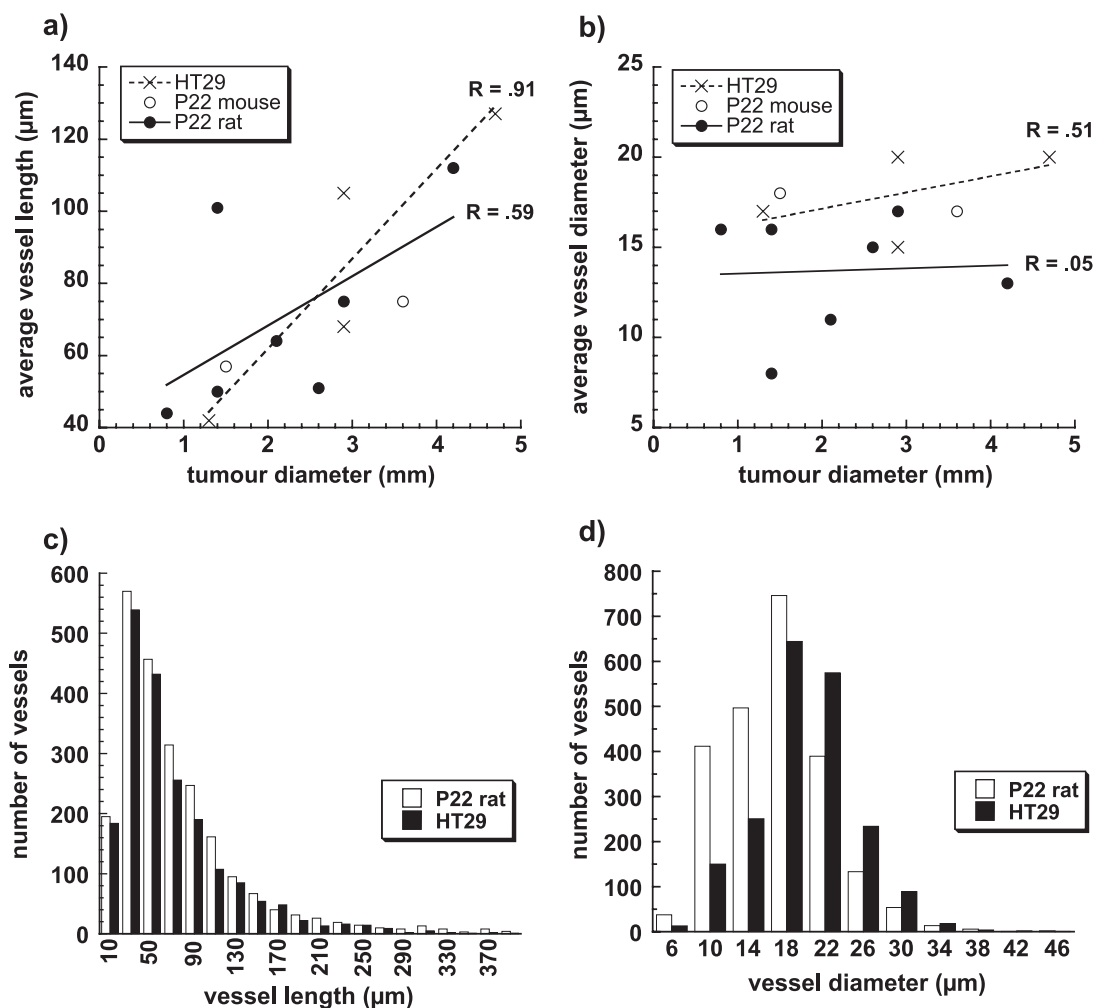
Fig. 4. Average vessel length (a) but not diameter (b) tended to increase with increasing tumour size. Mean vessel diameter was significantly smaller for the P22 tumours than the HT29 tumours. Regression lines and coefficients apply to HT29 tumours (dashed line) and P22 tumours growing in rats (solid line). Histograms in (c) and (d) represent a single tumour of each type (HT29: 3.0×2.3 mm with 2026 vessels; P22: 1.9×2.3 mm with 2328 vessels).

between the two tumour types. However, the average vessel diameter and average interstitial distance (Figs. 4 and 7) were significantly lower in the P22 tumours than in the HT29 tumours ($P<0.05$ for the difference between the means of all tumours in each group; Student's t-test). Interestingly, although the tortuosity and fractal dimensions were not significantly different in the two tumour types overall, both parameters tended to decrease with tumour size in the HT29 tumours, whereas they remained constant for the P22 tumours (Fig. 7). This reflects the different patterns of

vascularization observed for the two tumour types. As shown in Fig. 3, there is a band of highly vascularized tissue at the periphery of HT29 tumours, with vessels extending into the tumour centre. As tumours grow, the tortuous vessels in the highly vascularized peripheral band will contribute relatively less to the overall measurements, with a subsequent decrease in overall vessel tortuosity with increased tumour size. In contrast, vascular networks in the P22 tumour are more homogeneously organized within the tumour mass.
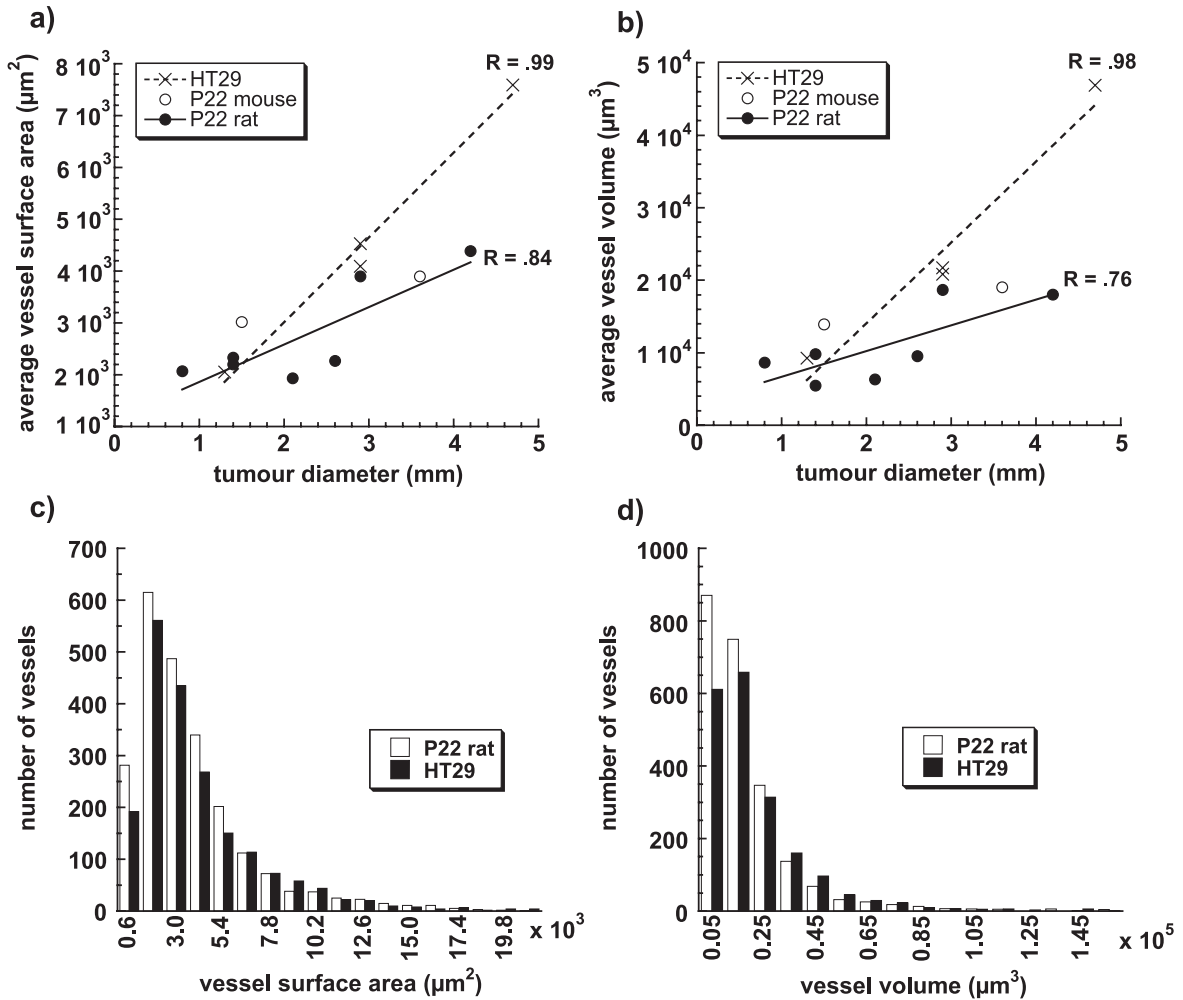
Fig. 5. Average vascular surface area (a) and volume (b) tended to increase with tumour size as a result of an increase in vascular length (Fig. 4). There was no significant difference in these parameters between the two tumour types. Regression lines are plotted as in Fig. 4. Histograms in (c) and (d) represent the same tumours as shown in Fig. 4.

Analysis of fractal dimensions of the vasculature in growing tumours can inform on the nature of the driving forces for angiogenesis and the efficiency of the blood supply for drug delivery in established networks [52]. The fractal dimension describes the self-similar nature of a network and, in a normal capillary network, reflects a space-filling (compact) structure (fractal dimension of 3.00 in 3D and 2.00 in 2D) [52]. The fractal dimensions of the P22 and HT29 tumours were both significantly lower than 3.00 (Fig. 7), indicating a significant difference from normal. In a previous publication, we found that

projecting the 3D vascular networks of sample P22 and HT29 tumour networks onto a 2D plane gave fractal dimensions that were very close to theoretical values for a "percolation" and "diffusion-limited" model of tumour angiogenesis for the two tumour types, respectively [41]. The fractal dimensions calculated from the full 3D images, as used in the current study (Fig. 7), are rather lower than the theoretical values for these models and, as discussed previously, are probably a reflection of the fact that tumour growth is somewhat confined in two dimensions within the window chamber [41].
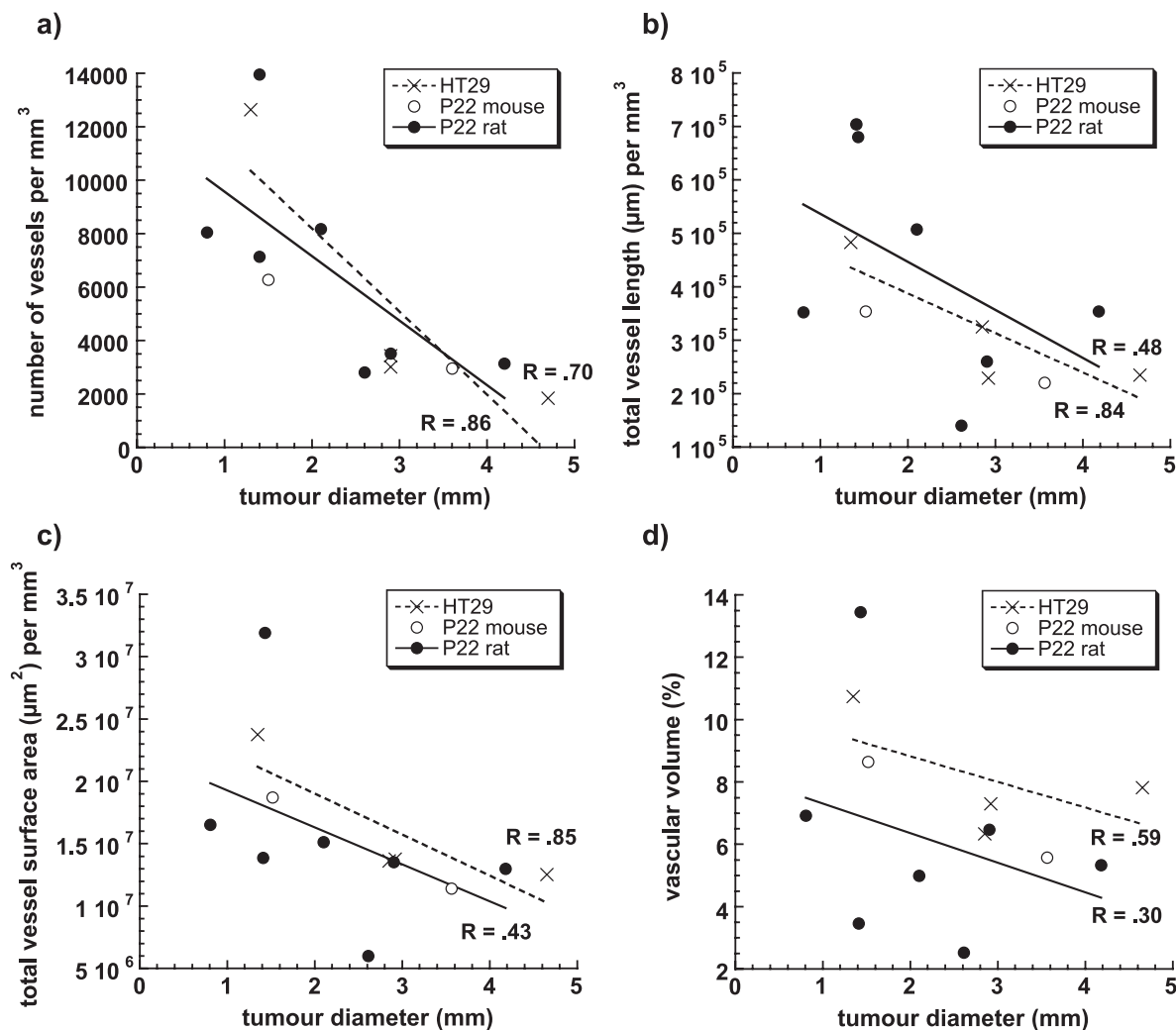
Fig. 6. Total vessel counts per mm³ tumour tended to decrease with tumour size (a). However, due to individual vessels lengthening with increased tumour size (Fig. 4), total vascular length density (b) was less affected by tumour size. Total vascular surface area density (c) and vascular volume density (d) are even less affected by tumour size because of the influence of vessel diameter (which does not change with tumour size, Fig. 4) on these calculated values. Regression lines are plotted as in Fig. 4.

Description of the vascular networks in the P22 tumour as fitting a "percolation" model is consistent with results for two other tumour types studied in this way [52] and implies that growth occurs in response to a random local property of the growth substrate. The driving forces for "diffusion-limited" angiogenesis could be physical variables such as pressure or concentration gradients of angiogenic factors, for example. These preliminary studies illustrate the potential power of fractal analysis not only for describing the vascular patterning in tumours but also for helping to understand the controlling factors in tumour angiogenesis.

These observed differences in vascular morphology between the tumour types may contribute to their different sensitivities to CA-4-P. Further studies investigating potential differences in vascular function and peri-endothelial cell support between tumours with very different sensitivities to CA-4-P are currently in progress.

5.3. Vascular permeability

Fig. 8 illustrates measurement of leakage of 40 kDa dextran from the vasculature of the P22 tumour growing in the rat. In the examples illustrated, K_i for leakage of dextran from the tumour vasculature of the animal treated with CA-4-P was approximately twice that in the untreated animal, suggesting that CA-4-P increases vascular permeability in the P22 tumour very rapidly after treatment. This result is typical of an extended study, in which tumour K_i was calculated for six treated and seven untreated rats (unpublished data). The lifetime of extravascular fluorescence was found to be the same as that of intravascular fluorescence (data not shown), suggesting that there are no significant differences between the local environments experienced by the fluorophore during transit through the vascular wall.

Since the diffusive permeability of unperturbed tumour blood vessels is usually very high, it is possible that the uptake of even high molecular weight compounds such as dextran is blood flow (rather than permeability) limited under certain circumstances. In this instance, K_i cannot be assumed to equate to PS but rather will approach the tissue blood flow rate. However, the increase in K_i in the CA-4-P-treated animal cannot be interpreted as an increase in tumour blood flow rate during the time-course of the experiment because we have extensive data demonstrating a rapid and profound decrease in blood flow rate following CA-4-P treatment in this window chamber model of the P22 tumour [45]. It follows that, if uptake of FITC dextran into the P22 tumour is influenced by blood flow rate under the conditions of this experiment, the K_i values obtained will underestimate the true value of PS and its increase after CA-4-P treatment. Furthermore, previous experiments have

Fig. 7. The average distance in the interstitium to the nearest capillary (a) tended to increase with tumour size in both tumour types. This parameter was also significantly smaller in the P22 tumours than in the HT29 tumours. The tortuosity of vessels (b) and fractal dimension of vascular networks (c) tended to decrease with tumour size in the HT29 tumours, whereas these parameters remained relatively constant with tumour size for the P22 tumours. Regression lines are plotted as in Fig. 4.
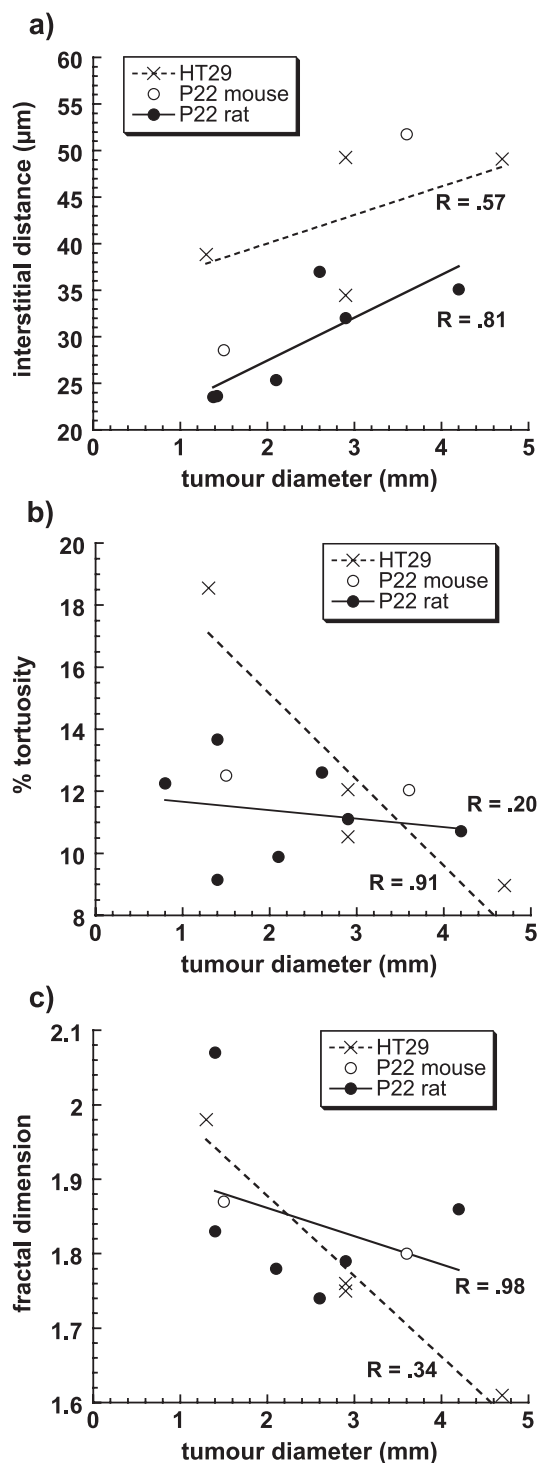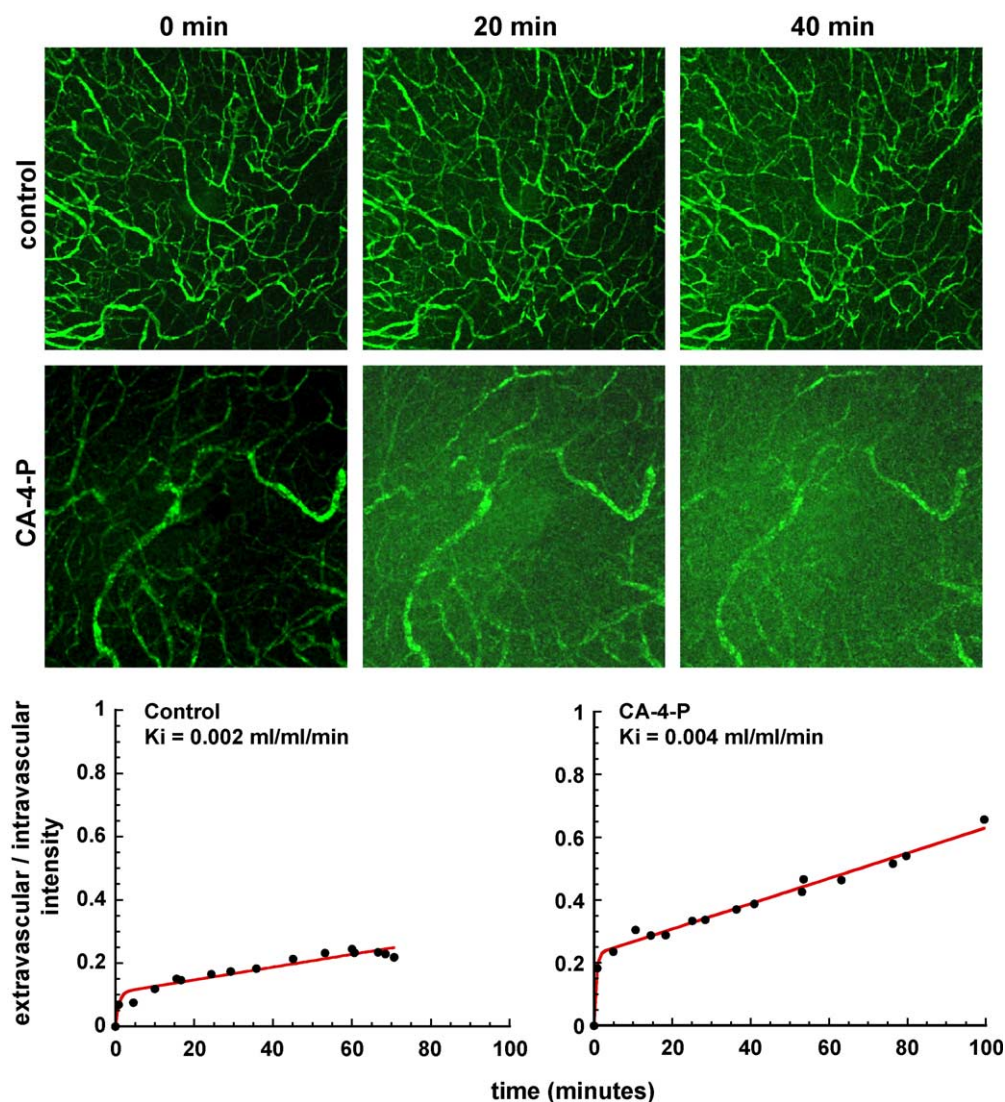
Fig. 8. CA-4-P increases vascular permeability to 40 kDa dextran in the P22 tumour in rats. Images show leakage of 40 kDa FITC–dextran from the tumour vasculature at selected time-points in a control tumour and a tumour in a CA-4-P-treated rat, which are representative of tumours from a larger group (vessel diameter 6–35 μm). Graphs show Patlak plots of vascular leakage of dextran from a single vessel from each of the two tumours shown.

shown that, on average, the diameter of tumour blood vessels does not change significantly within 1 h after this dose of CA-4-P [45], suggesting that an increase in the vascular surface area (S) could not account for the increase in K_i. Finally, it should be mentioned that the term P strictly corresponds to an 'apparent' permeability term reflecting the fact that leakage of dextran probably occurs via convection (movement along hydraulic and osmotic pressure gradients) as well as via diffusion along concentration gradients across the vascular wall. Therefore, it is not possible to determine, from the measured increase in K_i, whether CA-4-P treatment is causing physico-chemical changes in the vascular wall affecting dextran's diffusion or convection or both. These preliminary data illustrate the potential for

multi-photon microscopy for the assessment of apparent tumour vascular permeability–vascular surface area product (*PS* product) in vivo.

6. Conclusions

Multi-photon fluorescence microscopy is a technique that can be successfully applied to the investigation of vascular morphology and function of tumours growing in transparent window chambers. The ability to carry out repeat observations within individual tumours is a major advantage of this technique over previously available methods for investigating tumour vascular morphology in three dimensions. Repeat observations demonstrated a degree of vascular remodelling that is clearly an important part of tumour development. Techniques for quantifying vascular parameters in 3D images of tumour vascular networks were applied to two tumour types, revealing several differences that could be associated with their different responses to the tumour vascular targeting agent, CA-4-P. Vascular remodelling during tumour growth was also confirmed by the analysis of vascular parameters as a function of tumour size. Fractal analysis provided not only a mathematical description of tumour vascular network patterns but also a means for helping to identify the factors controlling tumour angiogenesis. The utility of multi-photon microscopy for measuring tumour vascular function, as well as morphology, was demonstrated by measurement of the vascular leakage of 40 kDa dextran following CA-4-P treatment. CA-4-P was found to approximately double the apparent permeability–vascular surface area product of tumour blood vessels, which is consistent with the effects of the drug on endothelial cells in vitro and is likely to contribute to the blood flow shutdown observed for this agent.

As multi-photon techniques become more widely available, their utility for measuring tumour vascular morphology and function, repeatedly in the same tumour and in three dimensions, will find applications in a number of fields. In particular, measurement of vascular parameters is crucial for understanding the process of tumour angiogenesis and investigating methods for improving drug delivery and therapeutic targeting of the tumour vasculature.

Appendix A. Methods for animal experiments

All animal procedures were carried out in accordance with the UK Animals (Scientific Procedures) Act 1986 and with the approval of the Ethical Review Committee of the Gray Cancer Institute. Early generation transplants of the P22 rat carcinosarcoma were grown in transparent window chambers, surgically implanted into a dorsal skin-flap of male BDIX rats, as described previously [45] and based on a technique originally described by Papenfuss et al. [53]. Briefly, rats were anaesthetized and two circular areas of skin on opposing sides of a dorsal skin-flap were thinned to the fascia layer. These were sandwiched between two glass cover-slips spaced approximately 250 μm apart and held in an aluminium frame (window chamber, Fig. 1). A fragment of P22 tumour was placed on one fascial surface before closure of the chamber. This system allows optical access to the tumour, whilst providing mechanical protection and stability. Window chambers of the appropriate size for mice were implanted into SCID mice in a very similar fashion to that described for rats above, except that, due to the relative optical transparency of mouse skin, the epidermal layers and panniculus muscle of one skin layer were left intact and the tumour fragment was placed directly onto the muscle surface. All layers of skin on the opposite skin surface were surgically removed.

Rats were anaesthetized for experiments between 7 and 14 days following surgery, when tumours ranged

from 0.8 to 4.2 mm in diameter. Body temperature was monitored via a rectal temperature probe and maintained at 35–37 °C using a thermostatically controlled heating pad and lamp. A second temperature probe placed on the surface of the glass window was used to maintain window temperature between 32 and 34 °C. Mice were conscious and restrained in a plastic jig for intravital microscopy. Tumours were examined when they reached 0.8–4.7 mm in diameter (between 7 and 15 days following surgery).

Appendix B. Imaging methods for vascular morphology

Vascular contrast for imaging was provided by intravenous injection of a purified anionic dextran (70 kDa) conjugated to a fluorophore (Cascade Blue™ or FITC, Molecular Probes), at a dose of 40 mg/kg and an excitation wavelength of 800 or 890 nm. Because of its anionic nature and high molecular size, the fluorescent dye was principally confined to the plasma throughout the time-course of experiments. For most experiments, the whole tumour vasculature was imaged. This involved the collection of sequential stacks of images for all but the smallest tumours (the limiting field of view for a single stack using the $10\times$ objective is 1.3×1.3 mm). Each stack consisted of a variable number of slices in the x–y plane, 2 μm apart, and took approximately 13 min to acquire for a typical stack of 50 slices. Image stacks for the larger tumours were 'stitched together', as illustrated in Fig. 1, by means of a software application written in-house, which makes use of the LabWindows CVI programming tools and IMAQ Image Processing library (National Instruments, Newbury, UK). Briefly, the stitching procedure starts with selection of one image from each stack for two adjacent frames in the x-direction. The point of best positional match of the two frames is found using normalised cross-correlation of a narrow strip of pixels from the left-hand image, with a wider rectangle from the right-hand image. Since the best correlation is achieved using images that have well-defined features and high contrast at the edges to be joined, the images to be used are selected automatically on the basis of maximum variance in the region of interest. This process is repeated for all image stacks in the x- and y-directions and the correlation points found are used to join the images of each plane in turn, to give a single stack per tumour. The joins were improved using mean pixel blending in the frame overlap regions.

Appendix C. Measurement of vascular tortuosity, interstitial distances and fractal dimensions

The measurement of percentage tortuosity (T) was equivalent to that of Norrby [54] and is based on the distance between branching points along the vasculature (L) and in a straight line (SP):

$$T = \left(1 - \frac{SP}{L}\right) \times 100$$

When measuring tissue vascularization in thin histological sections, a variety of measures of intercapillary distance have been used [55]. However, these measurements are not sufficiently defined when moving to 3D. Measurement of intercapillary distance in 3D vascular casts of the tumour vasculature has relied on the operator choosing suitable vascular loops for measurement [56]. In order to avoid this subjectivity, we chose to measure the mean interstitial distance to the nearest vessel from every point in the tumour, which will be related to the intercapillary distance. Ideally, this is measured from every point (voxel) within the tumour mass and averaged. However, the processing time that this required was excessive and we chose to sample the distribution of distances by sampling at regular intervals through the data set, at the expense of a larger possible error in the measurement. A reasonable compromise was to sample every 10 voxels in each direction.

The fractal dimensions of the networks were measured using published C-language source code [57], which is an implementation of the fast box counting algorithm [58]. This measurement required the re-sampling of the network representations to finely spaced point sets. The representations were re-sampled at the imaging resolution, typically 512×512 pixels per slice, or appropriately larger for 'stitched' images.

Appendix D. Assessment of tumour vascular permeability

Collection of multi-photon fluorescence images (consisting of a single 3D stack of 11 slices, 5 μm apart, approximating to a depth of 50 μm from the tumour surface) was started 1 min after injection of 40 mg/kg purified 40 kDa dextran conjugated to fluorescein (FITC–dextran, Sigma) and then every 4 min for up to 1 h, at an excitation wavelength of 890 nm.

3D images were analyzed using AMIRA visualization and data analysis software (TGS, USA). Ten vessels from each tumour image were chosen for analysis on the basis of good image quality and substantial distance from neighbouring vessels. Diameters of the chosen blood vessels used in this analysis ranged from 6 to 35 μm. A region of interest was chosen for each vessel that contained both vascular tissue and adjacent tumour tissue on either side of the vessel. Following delineation of the blood vessel volume, average fluorescence intensities for all pixels inside and outside the vessel were quantified, in 3D, over the time-course of the experiment. Results were plotted as the ratio of extravascular to intravascular fluorescence intensity (I_e/I_i) versus a transformed time axis, which equates to a plot of the I_e/I_i values that would have pertained had there been a constant input function (constant I_i) over the time-course of the experiment [59]. The transfer constant, K_i, describing the clearance of FITC–dextran from the plasma in ml blood cleared per ml tissue per minute, was calculated from the gradient of the straight-line portion of the curve. Assuming that tumour vascular leakage of FITC–dextran is permeability-limited, K_i approximates the apparent vascular permeability–vascular surface area product, PS. The term 'apparent' is used to indicate that extravasation of dextran probably occurs via convection along hydraulic and osmotic pressure gradients, as well as via diffusion along concentration gradients.

References

[1] N. Ferrara, H.-P. Gerber, J. LeCouter, The biology of VEGF and its receptors, Nat. Med. 9 (2003) 669–676.

[2] J. Folkman, Angiogenesis and angiogenesis inhibition: an overview, in: I.D. Goldberg, E.M. Rosen (Eds.), Regulation of Angiogenesis, Birkhäuser Verlag, Basel, 1997, pp. 1–8.

[3] H.F. Dvorak, J.A. Nagy, J.T. Dvorak, A.M. Dvorak, Identification and characterization of the blood vessels of solid tumors that are leaky to circulating macromolecules, Am. J. Pathol. 133 (1988) 95–109.

[4] A. Eberhard, S. Kahlert, V. Goede, B. Hemmerlein, K.H. Plate, H.G. Augustin, Heterogeneity of angiogenesis and blood vessel maturation in human tumors: implications for antiangiogenic tumor therapies, Cancer Res. 60 (2000) 1388–1393.

[5] S. Paku, N. Paweletz, First steps of tumor-related angiogenesis, Lab. Invest. 65 (1991) 334–346.

[6] R.K. Jain, Transport of molecules across tumor vasculature, Cancer Metastasis. Rev. 6 (1987) 559–593.

[7] H.F. Dvorak, J.A. Nagy, A.M. Dvorak, Structure of solid tumors and their vasculature: implications for therapy with monoclonal antibodies, Cancer Cells 3 (1991) 77–85.

[8] Y. Boucher, L.T. Baxter, R.K. Jain, Interstitial pressure gradients in tissue-isolated and subcutaneous tumors: implications for therapy, Cancer Res. 50 (1990) 4478–4484.

[9] J.R. Less, T.C. Skalak, E.M. Sevick, R.K. Jain, Microvascular architecture in a mammary carcinoma: branching patterns and vessel dimensions, Cancer Res. 51 (1991) 265–273.

[10] R.J. Gillies, P.A. Schornack, T.W. Secomb, N. Raghunand, Causes and effects of heterogenous perfusion in tumors, Neoplasia 1 (1999) 197–207.

[11] M.A. Konerding, W. Malkusch, B. Klapthor, C. van Ackern, E. Fait, S.A. Hill, C. Parkins, D.J. Chaplin, M. Presta, J. Denekamp, Evidence for characteristic vascular patterns in solid tumours: quantitative studies using corrosion casts, Br. J. Cancer 80 (1999) 724–732.

[12] D.J. Chaplin, P.L. Olive, R.E. Durand, Intermittent blood flow in a murine tumor: radiobiological effects, Cancer Res. 47 (1987) 597–601.

[13] G.M. Tozer, S. Lewis, A. Michalowski, V. Aber, The relationship between regional variations in blood flow and histology in a transplanted rat fibrosarcoma, Br. J. Cancer 61 (1990) 250–257.

[14] M. Hockel, P. Vaupel, Biological consequences of tumor hypoxia, Semin. Oncol. 28 (2001) 36–41.

[15] M. Hockel, K. Schlenger, B. Aral, M. Mitze, U. Schaffer, P. Vaupel, Association between tumor hypoxia and malignant progression in advanced cancer of the uterine cervix, Cancer Res. 56 (1996) 4509–4515.

[16] A.W. Fyles, M. Milosevic, R. Wong, M.C. Kavanagh, M. Pintilie, A. Sun, W. Chapman, W. Levin, L. Manchul, T.J. Keane, R.P. Hill, Oxygenation predicts radiation response and survival in patients with cervix cancer, Radiother. Oncol. 48 (1998) 149–156.

[17] J. Denekamp, Endothelial cell proliferation as a novel approach to targeting tumour therapy, Br. J. Cancer 45 (1982) 136–139.

[18] D.J. Chaplin, G.J. Dougherty, Tumour vasculature as a target for cancer therapy, Br. J. Cancer 80 (Suppl. 1) (1999) 57–64.

[19] M.W. Dewhirst, C. Gustafson, J.F. Gross, C.Y. Tso, Temporal effects of 5.0 Gy radiation in healing subcutaneous micro-

vasculature of a dorsal flap window chamber, Radiat. Res. 112 (1987) 581–591.

[20] R.M. Foltz, R.E. McLendon, H.S. Friedman, R.K. Dodge, D.D. Bigner, M.W. Dewhirst, A pial window model for the intracranial study of human glioma microvascular function, Neurosurgery 36 (1995) 976–985.

[21] S. Patan, S. Tanda, S. Roberge, R.C. Jones, R.K. Jain, L.L. Munn, Vascular morphogenesis and remodeling in a human tumor xenograft: blood vessel formation and growth after ovariectomy and tumor implantation, Circ. Res. 89 (2001) 732–739.

[22] J.S. Condeelis, J. Wyckoff, J.E. Segall, Imaging of cancer invasion and metastasis using green fluorescent protein, Eur. J. Cancer 36 (2000) 1671–1680.

[23] D.M. Foreman, S. Bagley, J. Moore, G.W. Ireland, D. McLeod, M.E. Boulton, Three dimensional analysis of the retinal vasculature using immunofluorescent staining and confocal laser scanning microscopy, Br. J. Ophthalmol. 80 (1996) 246–251.

[24] W. Denk, J.H. Strickler, W.W. Webb, Two-photon laser scanning fluorescence microscopy, Science 248 (1990) 73–76.

[25] D.R. Sandison, D.W. Piston, R.M. Williams, W.W. Webb, Quantitative comparison of background rejection, signal-to-noise ratio and resolution in confocal and full field laser scanning microscopes, Appl. Opt. 34 (1995) 3576–3588.

[26] W. Denk, K. Svoboda, Photon upmanship: why multiphoton imaging is more than a gimmick, Neuron 18 (1997) 351–357.

[27] J.M. Squirrell, D.L. Wokosin, J.G. White, B.D. Bavister, Long-term two-photon fluorescence imaging of mammalian embryos without compromising viability, Nat. Biotechnol. 17 (1999) 763–767.

[28] M. Straub, P. Lodemann, P. Holroyd, R. Jahn, S.W. Hell, Live cell imaging by multifocal multiphoton microscopy, Eur. J. Cell Biol. 79 (2000) 726–734.

[29] V. Andresen, A. Egner, S.W. Hell, Time-multiplexed multifocal multiphoton microscope, Opt. Lett. 26 (2001) 75–77.

[30] W. Denk, K.R. Delaney, A. Gelperin, D. Kleinfeld, B.W. Strowbridge, D.W. Tank, R. Yuste, Anatomical and functional imaging of neurons using 2-photon laser scanning microscopy, J. Neurosci. Methods 54 (1994) 151–162.

[31] K. Konig, I. Riemann, High-resolution multiphoton tomography of human skin with subcellular spatial resolution and picosecond time resolution, J. Biomed. Opt. 8 (2003) 432–439.

[32] D.W. Piston, Imaging living cells and tissues by two-photon excitation microscopy, Trends Cell Biol. 9 (1999) 66–69.

[33] B.R. Masters, P.T. So, E. Gratton, Multiphoton excitation microscopy of in vivo human skin. Functional and morphological optical biopsy based on three-dimensional imaging, lifetime measurements and fluorescence spectroscopy, Ann. N.Y. Acad. Sci. 838 (1998) 58–67.

[34] D.W. Piston, B.R. Masters, W.W. Webb, Three-dimensionally resolved NAD(P)H cellular metabolic redox imaging of the in situ cornea with two-photon excitation laser scanning microscopy, J. Microsc. 178 (1995) 20–27.

[35] E.B. Brown, R.B. Campbell, Y. Tsuzuki, L. Xu, P. Carmeliet, D. Fukumura, R.K. Jain, In vivo measurement of gene expression, angiogenesis and physiological functions in tumors using multiphoton laser scanning microscopy, Nat. Med. 7 (2001) 864–868.

[36] S.M. Ameer-beg, P.R. Barber, R.J. Hodgkiss, R.J. Locke, R.G. Newman, G.M. Tozer, B. Vojnovic, J. Wilson, Application of multiphoton steady-state and lifetime imaging to mapping of tumour vascular architecture in vivo, Proc. SPIE 4620 (2002) 85–95.

[37] G. Alexandrakis, E.B. Brown, R.T. Tong, T.D. McKee, R.B. Campbell, Y. Boucher, R.K. Jain, Two-photon fluorescence correlation microscopy reveals the two-phase nature of transport in tumors, Nat. Med. 10 (2004) 203–207.

[38] I. Garkavtsev, S.V. Kozin, O. Chernova, L. Xu, F. Winkler, E. Brown, G.H. Barnett, R.K. Jain, The candidate tumour suppressor protein ING4 regulates brain tumour growth and angiogenesis, Nature 428 (2004) 328–332.

[39] M.A. Abdul-Karim, K. Al-Kofahi, E.B. Brown, R.K. Jain, B. Roysam, Automated tracing and change analysis of angiogenic vasculature from in vivo multiphoton confocal image time series, Microvasc. Res. 66 (2003) 113–125.

[40] P.R. Barber, B. Vojnovic, S.M. Ameer-Beg, R.J. Hodgkiss, G.M. Tozer, J. Wilson, Semi-automated software for the three-dimensional delineation of complex vascular networks, J. Microsc. 211 (2003) 54–62.

[41] P.R. Barber, S.M. Ameer-Beg, B. Vojnovic, R.J. Hodgkiss, G.M. Tozer, J. Wilson, Three-dimensional imaging and quantification of complex vascular networks, in: Proc. SPIE, vol. 5139, 2003, pp. 67–78.

[42] S.M. Galbraith, R.J. Maxwell, M.A. Lodge, G.M. Tozer, J. Wilson, N.J. Taylor, J. Stirling, L. Sena, A.R. Padhani, G.J.S. Rustin, Combretastatin A4 phosphate has tumor anti-vascular activity in rat and man demonstrated by dynamic MRI, J. Clin. Oncol. 21 (2003) 2831–2842.

[43] C. Kanthou, G.M. Tozer, The tumor vascular targeting agent combretastatin A-4-phosphate induces reorganization of the actin cytoskeleton and early membrane blebbing in human endothelial cells, Blood 99 (2002) 2060–2069.

[44] G.M. Tozer, C. Kanthou, C.S. Parkins, S.A. Hill, The biology of the combretastatins as tumour vascular targeting agents, Int. J. Exp. Pathol. 83 (2002) 21–38.

[45] G.M. Tozer, V.E. Prise, J. Wilson, M. Cemazar, S. Shan, M.W. Dewhirst, P.R. Barber, B. Vojnovic, D.J. Chaplin, Mechanisms associated with tumor vascular shut-down induced by combretastatin A-4 phosphate: intravital microscopy and measurement of vascular permeability, Cancer Res. 61 (2001) 6413–6422.

[46] V.E. Prise, D.J. Honess, M.R.L. Stratford, J. Wilson, G.M. Tozer, The vascular response of tumor and normal tissues in the rat to the vascular targeting agent, combretastatin A-4-phosphate, at clinically relevant doses, Int. J. Oncol. 21 (2002) 717–726.

[47] D.A. Beauregard, S.A. Hill, D.J. Chaplin, K.M. Brindle, The susceptibility of tumors to the antivascular drug combretastatin A4 phosphate correlates with vascular permeability, Cancer Res. 61 (2001) 6811–6815.

[48] R.K. Jain, Delivery of novel therapeutic agents into tumours: physiological barriers and strategies, J. Natl. Cancer Inst. 81 (1989) 570–576.

[49] F. Yuan, M. Leunig, D.A. Berk, R.K. Jain, Microvascular permeability of albumin, vascular surface area, and vascular volume measured in human adenocarcinoma LS174T using dorsal chamber in SCID mice, Microvasc. Res. 45 (1993) 269–289.

[50] C.Y. Li, S. Shan, Q. Huang, R.D. Braun, J. Lanzen, K. Hu, P. Lin, M.W. Dewhirst, Initial stages of tumor cell-induced angiogenesis: evaluation via skin window chambers in rodent models, J. Natl. Cancer Inst. 92 (2000) 143–147.

[51] P. Vajkoczy, M. Farhadi, A. Gaumann, R. Heidenreich, R. Erber, A. Wunder, J.C. Tonn, M.D. Menger, G. Breier, Microtumor growth initiates angiogenic sprouting with simultaneous expression of VEGF, VEGF receptor-2, and angiopoietin-2, J. Clin. Invest. 109 (2002) 777–785.

[52] Y. Gazit, J.W. Baish, N. Safabakhsh, M. Leunig, L.T. Baxter, R.K. Jain, Fractal characteristics of tumor vascular architecture during tumor growth and regression, Microcirculation 4 (1997) 395–402.

[53] H.D. Papenfuss, J.F. Gross, M. Intaglietta, F.A. Treese, A transparent access chamber for the rat dorsal skin fold, Microvasc. Res. 18 (1979) 311–318.

[54] K. Norrby, Microvascular density in terms of number and length of microvessel segments per unit tissue volume in mammalian angiogenesis, Microvasc. Res. 55 (1998) 43–53.

[55] C.M. West, R.A. Cooper, J.A. Loncaster, D.P. Wilks, M. Bromley, Tumor vascularity: a histological measure of angiogenesis and hypoxia, Cancer Res. 61 (2001) 2907–2910.

[56] W. Malkusch, M.A. Konerding, B. Klapthor, J. Bruch, A simple and accurate method for 3-D measurements in microcorrosion casts illustrated with tumour vascularization, Anal. Cell. Pathol. 9 (1995) 69–81.

[57] J.J. Sarraille, L.S. Myers, Fd3—a program for measuring fractal dimension, Educ. Psychol. Meas. 54 (1994) 94–97.

[58] L.S. Liebovitch, T. Toth, A fast algorithm to determine fractal dimensions by box counting, Phys. Lett., A 141 (1989) 386–390.

[59] C.S. Patlak, R.G. Blasberg, J.D. Fenstermacher, Graphical evaluation of blood-to-brain transfer constants from multiple-time uptake data, J. Cereb. Blood Flow Metab. 3 (1983) 1–7.